Supplementary Information

Shiro Ihara[a], Mizumo Yoshinaga[b], Hiroya Miyazaki[c], Kota Wada[b], Satoshi Hata[b,d], Hikaru Saito[a,e]* and Mitsuhiro Murayama[a,f,g]

a. Institute for Materials Chemistry and Engineering, Kyushu University, Fukuoka 816-8580, Japan

E-mail: saito.hikaru.961@m.kyushu-u.ac.jp

b. Interdisciplinary Graduate School of Engineering Sciences, Kyushu University, Fukuoka 816-8580, Japan

c. Mel-Build Corporation, Nishi-ku, Fukuoka 819-0052, Japan

d. The Ultramicroscopy Research Center, Kyushu University, Fukuoka 819-0395, Japan

e. Pan-Omics Data-Driven Research Innovation Center, Kyushu University, Fukuoka 816-8580, Japan

f. Department of Materials Science and Engineering, Virginia Tech, Blacksburg, VA 24061, USA

g. Reactor Materials and Mechanical Design Group, Energy and Environmental Directorate, Pacific Northwest National Laboratory, WA 99352, USA

In situ observation at room temperature without electron dose control

In this study, we performed the 4D observation at the standby temperature (ST) of 200°C under extremely reduced electron dose condition. Without setting the ST and electron dose control, the in situ observation for sintering behaviour was unsuccessful. Fig.S1 shows the result of in situ observation at room temperature without electron dose control. The "observed area" in the figure was observed for a while and the outside area was not observed before finishing the 800 °C of heating process. As shown in the Fig.S1, only the NPs in the outside area coalesced with adjacent NPs, while NPs inside the observed area remained as individual particles. The cause of failure would be hydrocarbon contamination, which is often triggered by the electron beam. Therefore, the heating at ST and the dose control during the observation were necessary to avoid contamination in this study.
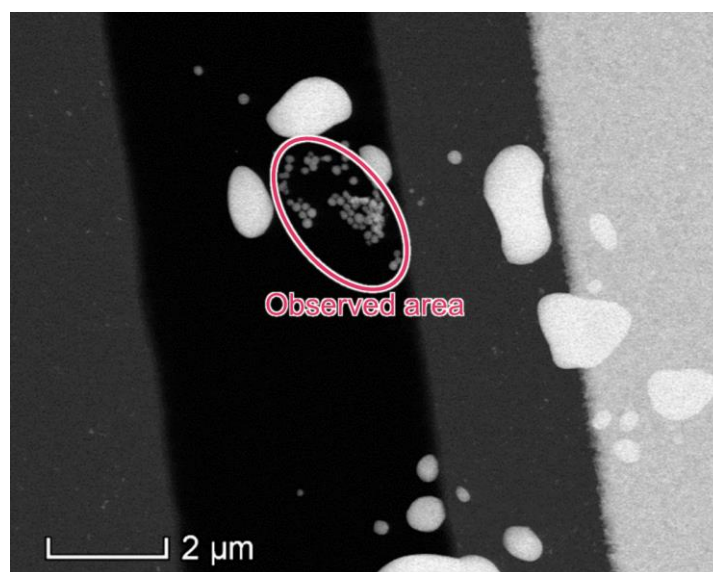

Fig.S1 Result of in situ observation at room temperature without electron dose control.

Heating log of 4D observation

Figure Sx2 shows the heating log when we perform the 4D observation. Since the time on processing temperature (PT) was too short compared to whole experiment time, the details of interval during the PT was highlighted. The overshoot from the processing temperature of 350℃ was recognized. Therefore, the median of temperature in each PT step was displayed in Fig.2. As indicated in the main body text, the sampling interval of the used software was 1 s, while the response time of the MEMS chip was less than 100 ms. Therefore, this study regarded the time on PT as the interval between the middle of time when increasing the temperature and the middle of time when decreasing the temperature, as shown in Fig.S2.
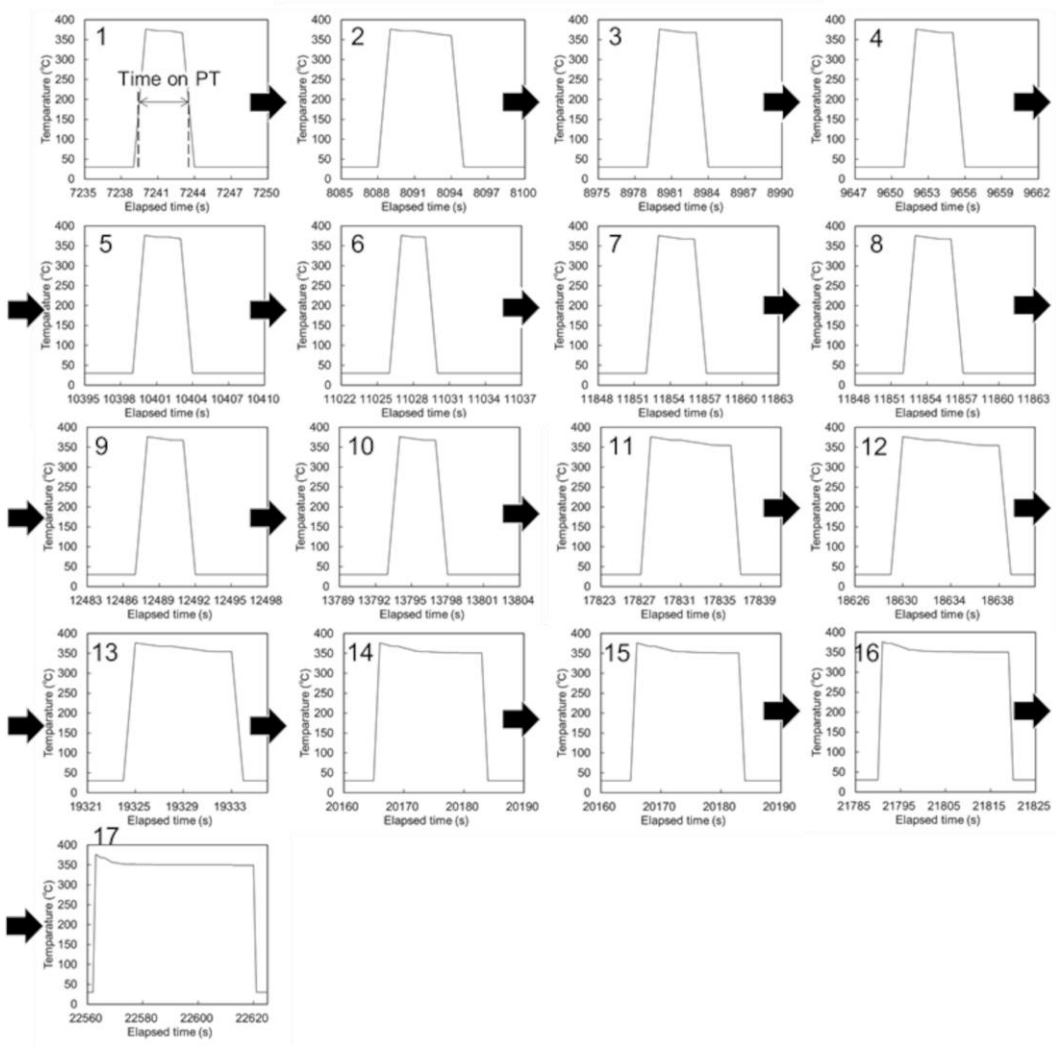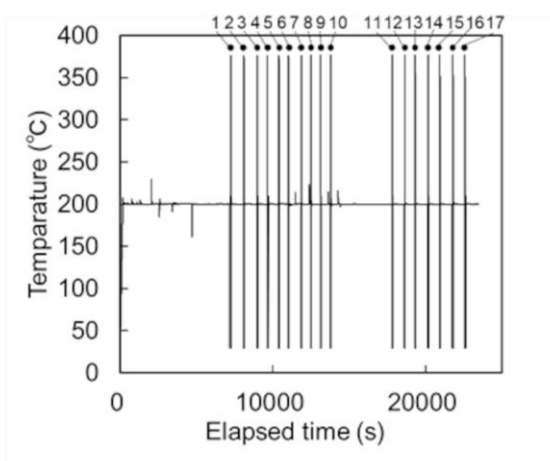
Fig.S2 Heating log in this study.

Denoising effect

To demonstrate the advantage of denoising effect, we performed additional observation in the same manner as the 4D observation under both low dose (2 pA) and high dose (140 pA) conditions, by using the high-angle triple-axis (HATA) holder[1]. Figure S3 shows representative tomograms extracted from each reconstructed tilt-series image and the low-dose series image processed by the BM3D. The figure demonstrates that the artefact is remarkably intense in the tomogram reconstructed from the low-dose images. These tomograms are to be binarized to distinguish the true signal and background, and thus the intensity of true signal and that of the artefact need to be clearly differentiated to guarantee the spatial resolution. To quantify the noise level, we calculated the signal ratio of Cu NPs and the artefact, which were respectively averaged in the selected area as shown in Fig.S3. The results are also shown in Fig.S3 bottom right, in which the denoising successfully recovers a high signal ratio.

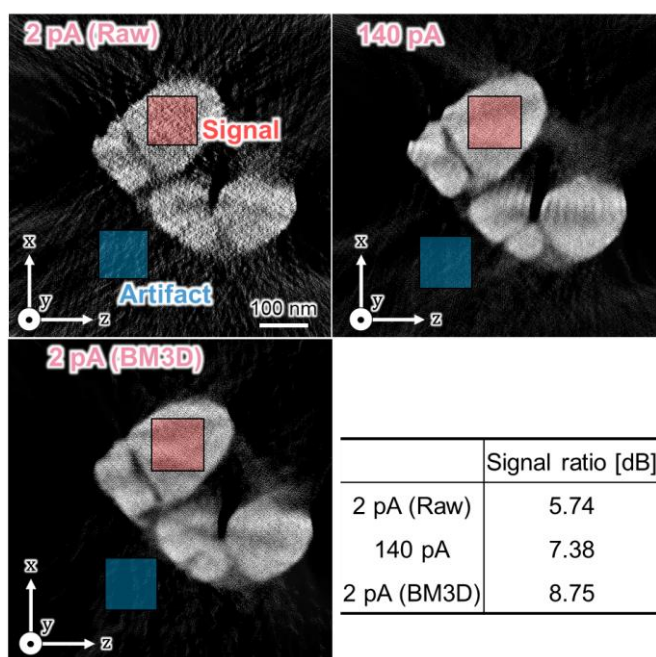|	Signal ratio [dB]
2 pA (Raw)	5.74
140 pA	7.38
2 pA (BM3D)	8.75

Fig.S3 Comparison of signal and artefact ratio in tomograms reconstructed from low and high electron dose, as well as low electron dose with BM3D processing. Note that the background intensity was ignored in each signal ratio calculation.

3D reconstruction artefact

Generally speaking, elongation along the projection direction in 3D reconstructed images, called missing wedge artefact [2,3], cannot be ignored when a tilt-series image is acquired with a limited tilt angle range because of insufficient coverage of 3D Fourier space[4]. The elongation is quantified as the

ratio of the length in the projection direction and the one in another direction. Theoretically, when the projection direction is along z-axis, the tilt axis is y-axis and another axis is x-axis, and the elongation factor e_{xz}, which is the ratio of the length in z and x direction, in a sphere reconstructed by simple back projection (SBP) is expressed as[5],

$$e_{xz} = \sqrt{\frac{\alpha + \sin \alpha \cos \alpha}{\alpha - \sin \alpha \cos \alpha}}, \tag{1}$$

where α [rad] is the maximum tilt angle. From Eq. (1), $e_{xz} = 2.41$ when the tilt angle was set to ±40°, which is the image acquisition condition in this study
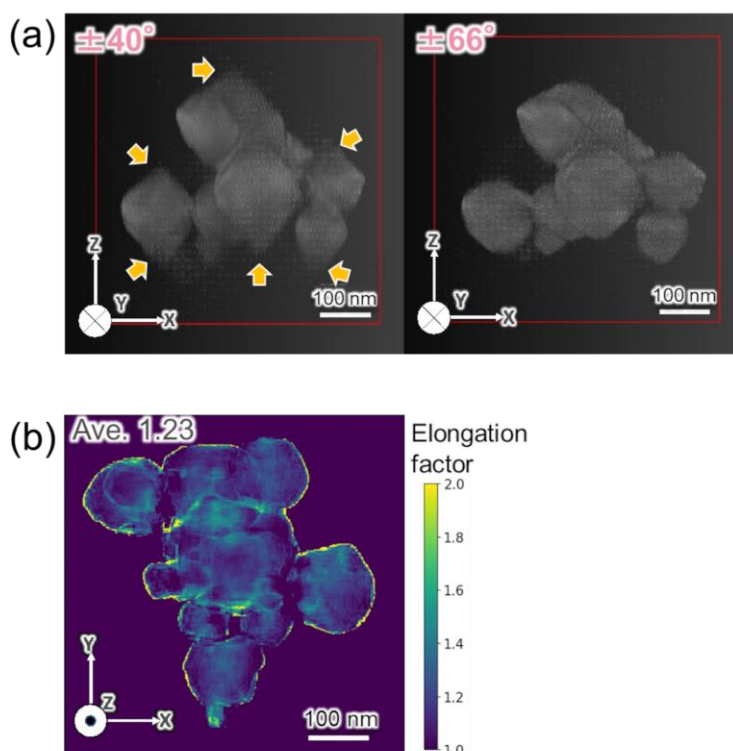

Fig.S4 Evaluation of 3D reconstruction artifact. Generally, the limitation of tilt angle range results in elongation along the projection direction (a). The elongation factor is quantified by superposing the two-3D data (b). Note that the elongation factor exceeding 2.0 is expressed as yellow in (b) to clearly visualize the distribution.

As for this study, a compressed sensing-based algorithm was employed in the reconstruction step to reduce the elongation, and thus the elongation was relatively low. Figure S4(a) shows the 3D images of the high dose (140 pA) in Fig.S3 but reconstructed with the tilt angle range of ±40° and ±66°, respectively. In the case of ±40°, the elongation along the z-direction was confirmed as highlighted by the yellow arrows. However, the diameter of NPs in x-direction stayed unchanged by changing the tilt angle range in this study. Therefore, the height in z-direction can be regarded as the elongation factor. By comparing the height in z-direction, we obtained the elongation factor distribution as shown

in Fig.S4(b). The elongation factor was 1.23 in average, which was considerably lower compared to the above mentioned two cases. Even if we define the elongation factor as the elongation from the $\pm 66°$ reconstruction, the ratio of e_{xz} between $\pm 40°$ and $\pm 66°$ in SBP and FBP become 1.72 and 1.44, respectively. Therefore, the compressed sensing-based reconstruction provides relatively high precision in z-direction for electron tomography.

Sintering behaviour with continuous heating

Since the Cu NPs experienced the multiple pulsed heating during the 4D observation, there would be a possibility that the sintering behavior differed from the case of continuous heating for the same total time on PT. For comparison, we performed an additional in situ observation for sintering with continuous heating. Figure S5 compares the STEM images obtained in the 4D observation (left) and the additional experiment (right). Note that the former has been processed by BM3D. The total time on PT was indicated on the upper left in each image. To account for the overshoot shown in Fig.S2, the PT was set to 370°C in the additional experiment. In Fig.S5, there were no significant difference in neck formation between the two images.
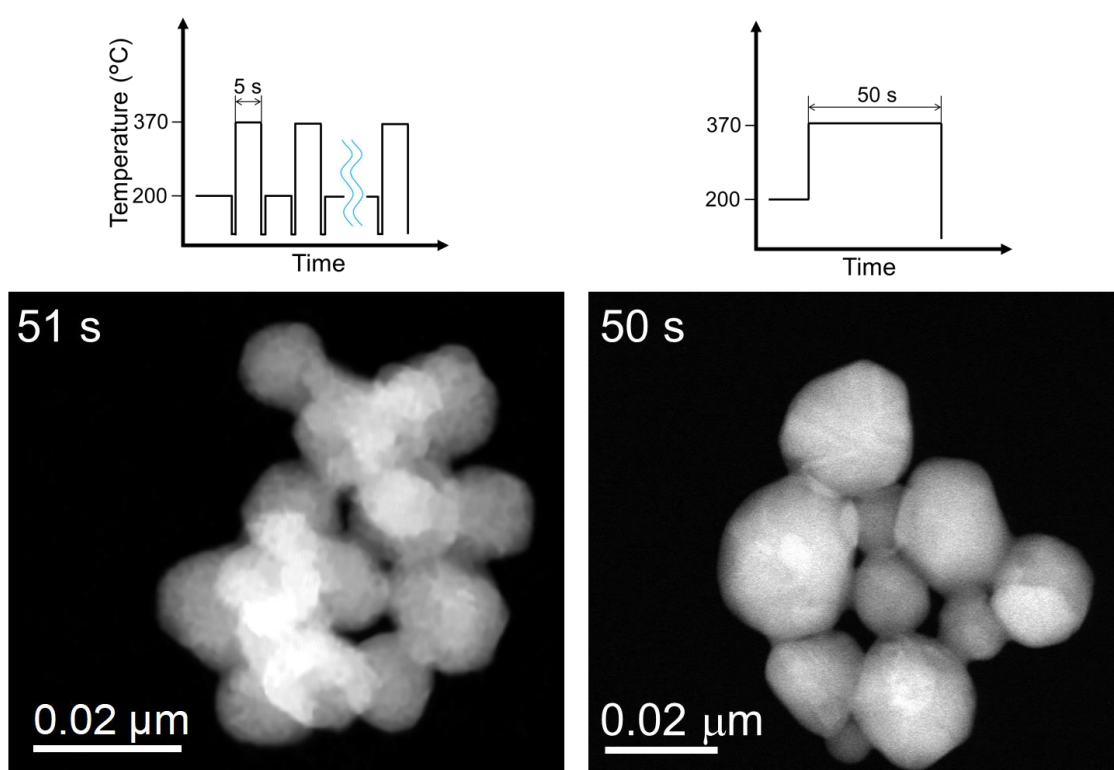

Fig.S5 Comparison of repeated heating (left) and continuous heating (right). The left

Sintering behaviour of Cu NPs in 3D

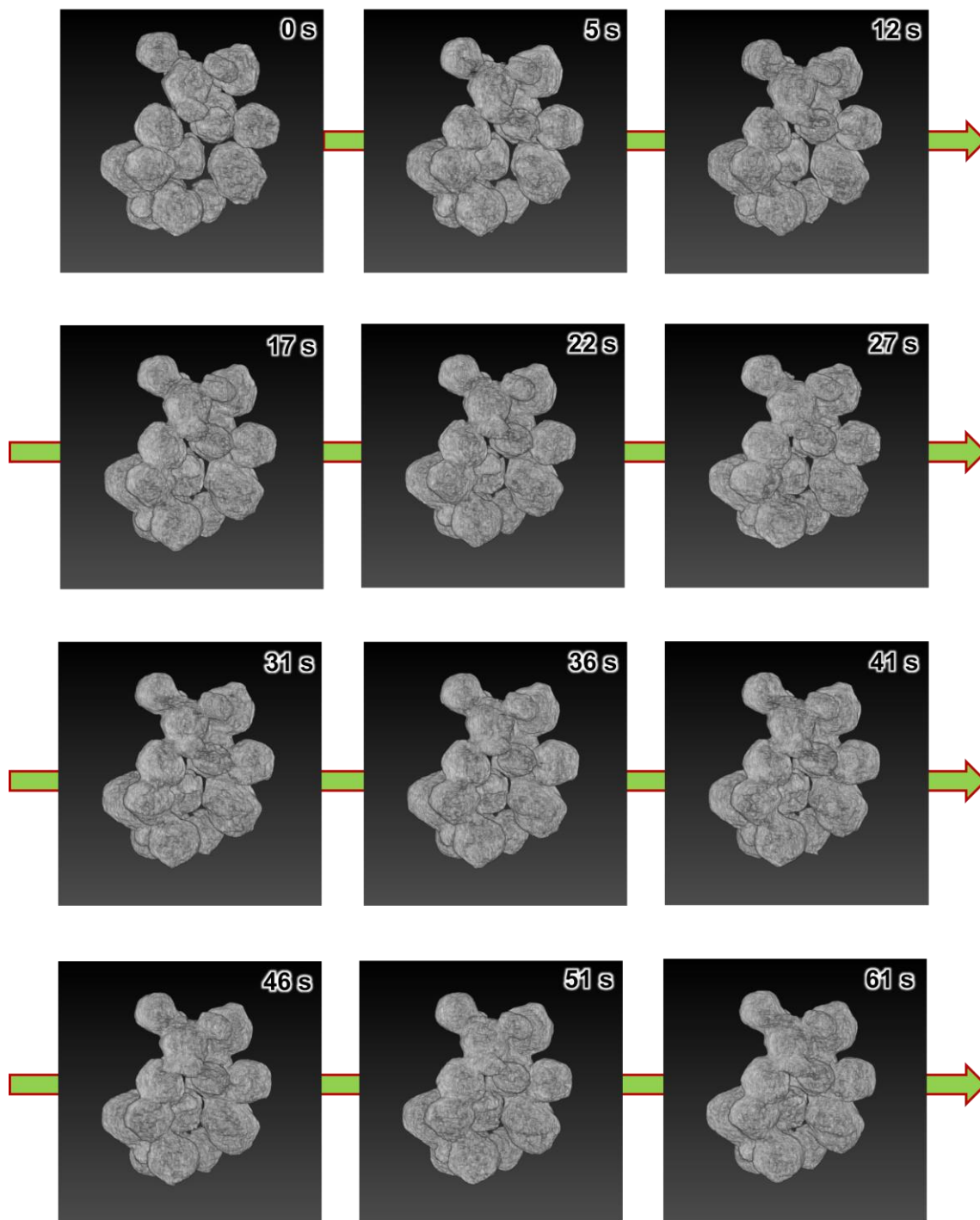Figure S6 shows the time-resolved sintering behaviour of Cu NPs obtained this study.

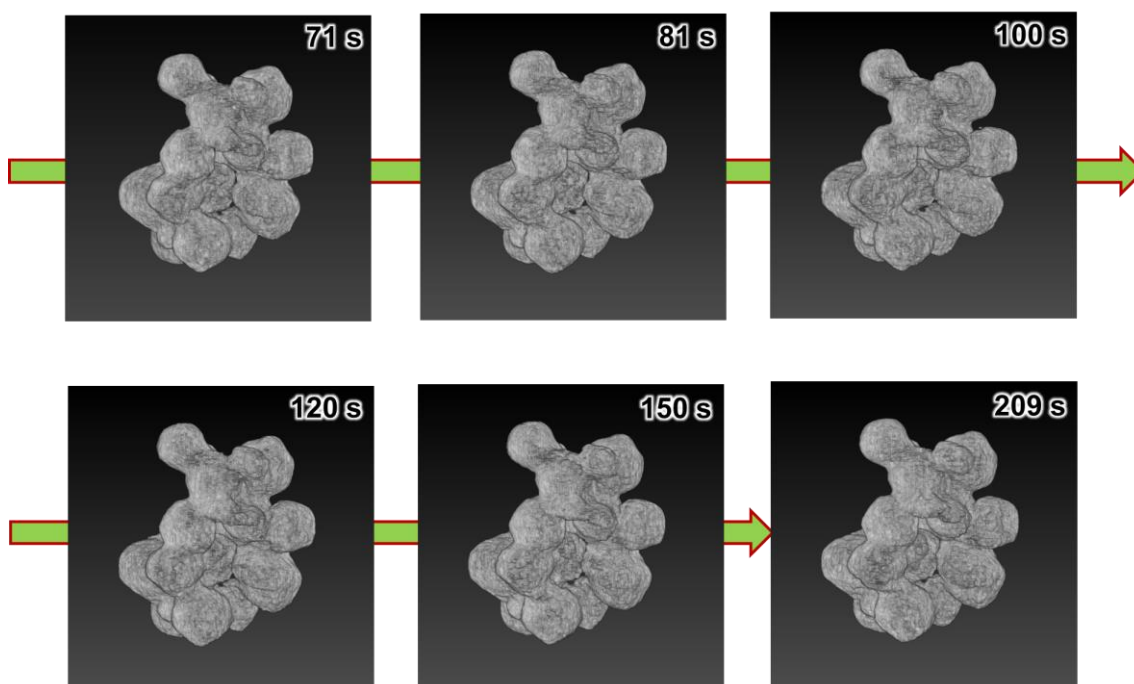Fig.S6 3D-reconstructed Cu NPs in sintering process.

Fig.S6 Continued.

Measurement of NPs in projection images

To evaluate the neck radius r_n, the distance between the centre of mass for each of targeted NP pairs in x-y plane (d_{xy}), the representative particle radius r_p, and also the representative NP's aspect ratio H/W, were evaluated through the procedure shown in Fig.S7. First, NPs that did not form neck (PNF) was removed from the image. Second, a NP that formed neck with the targeted NP (PF) was cut along the neck and removed. By separating along the neck and binarizing (threshold value was set to 60 in 8-bit images), we can draw a rectangle for each NP, which was utilized for evaluating H/W. r_n, d_{xy}, and r_p, were evaluated by using such obtained images.

1. Removing PNF

Removing the unnecessary area

2. Cutting and removing PF

Cutting along the neck.

3. Separating particle into two

Rotating neck to be horizontal to image

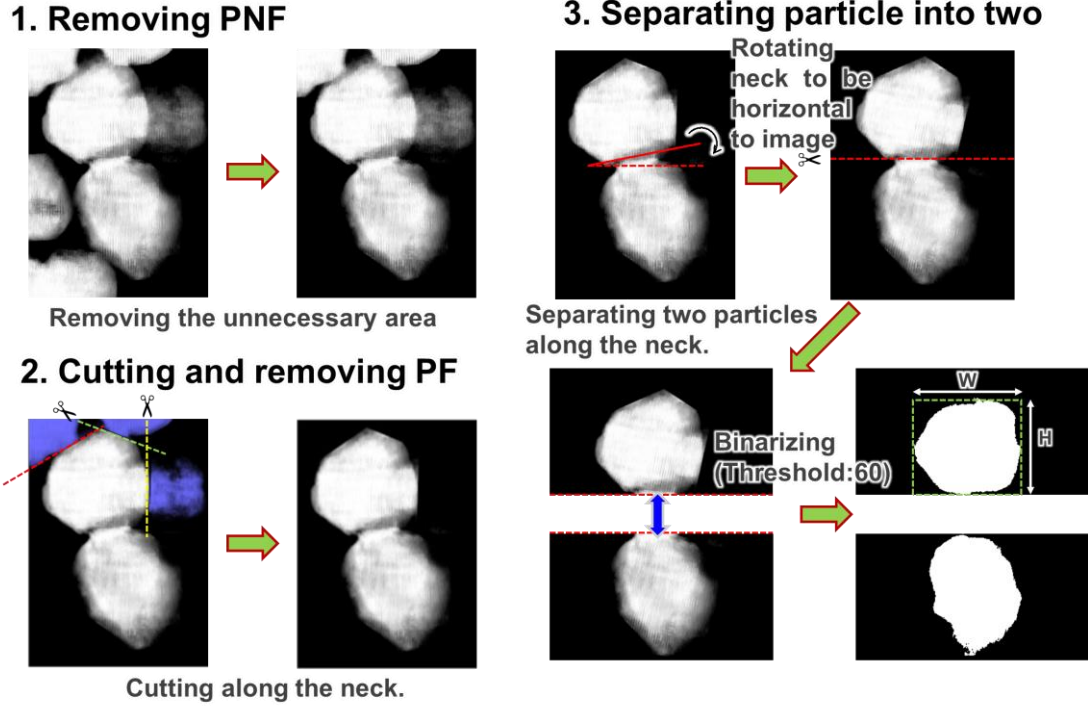Separating two particles along the neck.

Binarizing (Threshold:60)

Fig.S7 Schematic drawing of evaluation procedure for $r_n, d_{xy}, r_p,$ and $H/W.$

A mathematical model of sintering

The dashed curve plotted in main body text of Fig.9(a) was derived by approximating neck to a cylinder of equal volume. This model is illustrated in Fig.S8(a). In the figure, the sintered particles are approximated by truncated spheres and a cylinder, resulting in the dumbbell-like shape. The analytical expression of relationship between the neck width and the distance in-between the two spheres is derived by following process.

Let d and r_p be the particle distance and the particle radius, respectively. The central section of the particles overlapping each other is shown in Fig.S8(b). The overlapped range is to be cut at the edge of the neighboring circle (the hatched area in Fig.S8(b) middle) and is replaced to a cylinder with same volume. The volume of the region V_s is expressed as,

$$V_s = \pi \left(\frac{4}{3} r_p^3 - r_p d^2 + \frac{1}{3} d^3 \right),$$

while that of the cylinder V_c is

$$V_c = \pi r_n^2 h,$$

where r_n is the neck radius, h is height of the cylinder. From our definition,

$$2\{(d - r_p) + h\} = d$$

holds. Therefore,

$$V_c = \pi r_n^2 (r_p - \frac{d}{2})$$

Since $V_s = V_c$, we obtain

$$\left(\frac{r_n}{r_p}\right)^2 = \frac{4 - 4\left(\frac{d}{2r_p}\right)^2 + \frac{8}{3}\left(\frac{d}{2r_p}\right)^3}{3\left(1 - \frac{d}{2r_p}\right)}$$

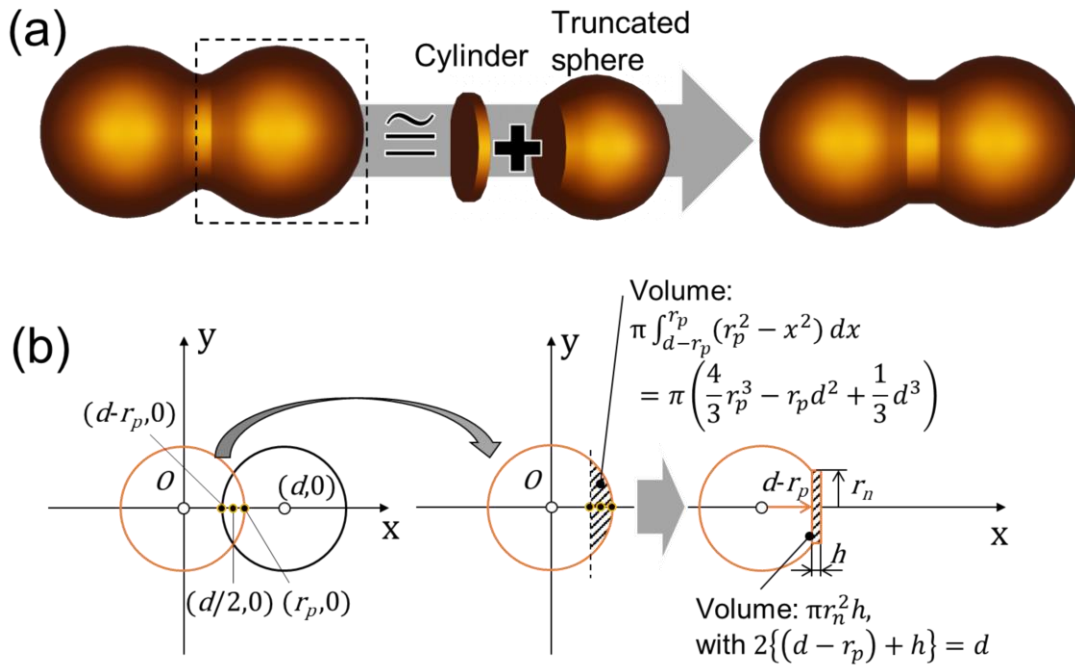This equation yielded the plot in Fig.9(a).

Fig.S8 (a) Schematic of a simplified sintering model. (b) Central section of overlapped particles, and calculation process of volume for truncating area and a cylinder.

References

1 S. Hata, H. Miyazaki, S. Miyazaki, M. Mitsuhara, M. Tanaka, K. Kaneko, K. Higashida, K. Ikeda, H. Nakashima, S. Matsumura, J. Barnard, J. Sharp and P. Midgley, *Ultramicroscopy,* 2011, **111**, 1168-1175.

2 M. Weyland, P. A. Midgley and J. M. Thomas, *J. Phys. Chem. B,* 2001, **105**, 7882-7886.

3 N. Kawase, M. Kato, H. Nishioka and H. Jinnai, *Ultramicroscopy,* 2007, **107**, 8-15.

4 J. E. Frank, *Electron tomography: methods for three-dimensional visualization of structures in the cell,* Springer, 2010.

5 M. Radermacher, *J. Electron Microsco. Tech.,* 1988, **9**, 359-394.